Temperature-Driven Reversible Rippling and Bonding of a Graphene Superlattice

Andrea Locatelli,[†,*] Chun Wang,[‡] Cristina Africh,[§] Nataša Stojić,[‡,⊥] Tevfik Onur Menteş,[†] Giovanni Comelli,[†,§,∥] and Nadia Binggeli[‡,⊥]

[†]Elettra - Sincrotrone Trieste, S.C.p.A., 34149 Trieste, Italy, [‡]Abdus Salam International Centre for Theoretical Physics, 34151 Trieste, Italy, [§]IOM-CNR Laboratorio TASC, 34149 Trieste, Italy, [⊥]IOM-CNR Democritos, 34151 Trieste, Italy, and [∥]Department of Physics and CENMAT, University of Trieste, 34127 Trieste, Italy

ABSTRACT In order to unravel the complex interplay between substrate interactions and film configuration, we investigate and characterize graphene on a support with non-three-fold symmetry, the square Ir(100). Below 500 °C, distinct physisorbed and chemisorbed graphene phases coexist on the surface, respectively characterized by flat and buckled morphology. They organize into alternating domains that extend on mesoscopic lengths, relieving the strain due to the different thermal expansion of film and substrate. The chemisorbed phase exhibits exceptionally large one-dimensional ripples with regular nanometer periodicity and can be reversibly transformed into physisorbed graphene in a temperature-controlled process that involves surprisingly few C—Ir bonds. The formation and rupture of these bonds, rather than ripples or strain, are found to profoundly alter the local electronic structure, changing graphene behavior from semimetal to metallic type. The exploitation of such subtle interfacial changes opens new possibilities for tuning the properties of this unique material.

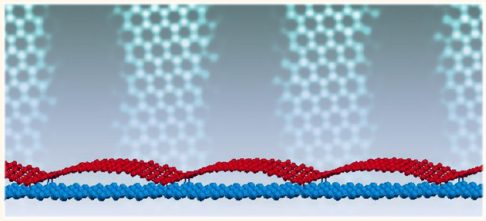

KEYWORDS: graphene · flat · buckled · rippling · Ir(100) · electronic structure · LEEM · XPEEM · STM · *ab initio*

The study of the graphene—metal interface has become a mainstream topic in materials science research, owing to its importance for the synthesis and exploitation of this sp^2-hybridized carbon network characterized by exceptional electron transport and other unique physical properties.[1,2] As a matter of fact, interfacial interactions play a key role in a number of fundamental processes that concern basic research, such as graphene growth and stability[3] or the fabrication of graphene-supported metallic nanostructures.[4] From the applications standpoint, accurate control over the metal—graphene interaction in heterostructures is crucial in both preserving and modifying the electronic properties of graphene, in order to enable their fruition in a variety of devices based on quantum architectures.[5,6]

Known since the early days of surface science,[7,8] epitaxial graphene has disclosed an unexpected variety of nanotextured morphologies and structures, which manifest the different nature and varying strength of the interactions occurring at the interface.[9] Among the most studied systems, single-layer graphene on fcc(111) or hcp(0001) transition metal surfaces exhibits a plethora of rotational structures and moiré patterns, which stem from the small lattice mismatch between graphene and substrate and are often accompanied by the formation of regular three-dimensional corrugations in the film.[10—12] It is now well-known that substrate interactions influence not only the film morphology but also, and most importantly, its electronic properties.[13—16] This concept has opened up the possibility to tune both doping and band gap in weakly coupled graphene systems,[17,18] either by choosing different metals as support[19] or by intercalating adspecies and buffer layers.[20] Conversely, the opposite condition of strong hybridization with metallic states may impact the π band, as occurs for monolayer graphene on Ni[21—23] and, even more dramatically, for Ru.[14]

The characterization of graphene on crystal faces with non-three-fold symmetry is gaining increasing scientific attention because of the notable properties exhibited by the grown film and future use of polycrystalline

* Address correspondence to andrea.locatelli@elettra.trieste.it.

Received for review April 30, 2013 and accepted July 19, 2013.

Published online July 19, 2013
10.1021/nn402178u

substrates for large-scale graphene synthesis. Notable examples are those of Cu(100),[24,25] due to the importance of this system for graphene transferring techniques, and Fe(110).[26] A peculiar aspect observed for graphene on Cu(100), in particular, is the formation of regular one-dimensional moiré structures with nanometer periodicity.[27−29] In the present work, we focus on graphene on a square symmetry support, Ir(100). Our work addresses the interplay between C−Ir bonding, film morphology, and electronic structure, with the aim of disentangling the effects of the film configuration and substrate interaction on the quasi-particle dispersion. A unique feature we find for this system is the occurrence of a reversible phase transformation between physisorbed and chemisorbed phases characterized by flat and buckled morphology. The latter exhibits exceptionally large one-dimensional ripples with a periodicity of 2.1 nm, closely resembling a structure recently observed for h-BN monolayer on Fe(110).[30] Owing to the challenges imposed by the size and different orientation of graphene domains, the complex structure of graphene on Ir was investigated using state-of-the-art experimental and theoretical tools, scanning tunneling microscopy (STM) for structural characterization at the atomic scale, and spectroscopic photoemission and low energy electron microscopy (SPELEEM)[31,32] at the mesoscale. The experimental results were substantiated by density functional theory (DFT) calculations for the determination of the atomic and electronic structure.

RESULTS AND DISCUSSION

In our experiments, graphene growth was monitored *in situ* using low energy electron microscopy (LEEM) and microprobe low energy electron diffraction (LEED). Similar to the case of graphene on Ir(111) and Ru(0001),[33] graphene on Ir(100) is obtained by thermal decomposition of ethylene at elevated sample temperatures. Briefly, the formation of a C adatom lattice gas readily lifts the Ir (1 × 5) reconstruction anticipating condensation, which occurs at step edges. Growth appears to be insensitive to the substrate morphology, the graphene lattice being undisrupted by steps and step bunches. Our LEED measurements show that the graphene lattice is preferentially aligned at few degrees off the Ir⟨001⟩. At variance with the case of graphene on Cu, no other orientations are observed, suggesting a stronger interaction with the substrate. We note, however, that the morphology and exact orientation of the graphene flakes depend notably on the growth temperature. For temperatures below 680 °C, the diffraction spots are rotationally broadened, the first-order diffraction exhibiting a width of about 4°. This indicates a poor rotational coherence between different flakes, which have typical size of less than a micrometer. With increasing temperature, the islands increase notably in size. At a growth temperature of 850 °C, the graphene lattice is aligned at about 3.5° with respect to Ir⟨001⟩. Different crystals exhibit an improved rotational coherence (±0.6° with respect to this value). In the experiments reported here, graphene was grown in the temperature range of 800−850 °C; the growth was interrupted by restoring UHV conditions when the crystal size was sufficiently large to enable microprobe characterization. Subsequently, the sample was rapidly cooled to room temperature.

The LEEM micrographs in Figure 1a illustrate the typical aspect of a graphene island at ambient temperature. The island extends for several micrometers and shows the coexistence of two distinct phases, labeled FG (flat graphene) and BG (buckled graphene), as will be justified below. The FG phase, appearing bright in the LEEM images, predominates on the other, which is embedded and forms elongated stripes that propagate over micrometer lengths, with a width of a few hundred nanometers. The stripes are aligned at 70−75° with respect to Ir⟨001⟩ and cover about 20% of the graphene surface. These stripes are not observed at high temperature, but they form during cooling to ambient temperature, nucleating at about 500 °C, as will be detailed later.

The LEED pattern of a graphene flake at room temperature is shown in Figure 1d. As can be seen, the diffraction pattern is characterized by the superposition of the six first-order diffraction beams of graphene (indicated by the red arrows) and numerous other spots forming a coincidence structure with Ir with a periodicity of 11 lattice units along Ir⟨001⟩. We examined 25 graphene flakes grown under the same conditions and observed the same structure in more than 65% of the cases. In the remaining cases, we observed closely related structures, the coincidence being a few degrees off the Ir⟨001⟩, resulting in a slight variation of its periodicity. A careful analysis of the LEED pattern shows that graphene first-order spots do not exactly match those of the coincidence structure (see the Supporting Information). Thus, we conclude that the graphene lattice is incommensurate to the substrate. In fact, the LEED of the FG phase exhibits a weak moiré pattern, originating from multiple scattering between the graphene lattice and the Ir lattice. The spot position is similar for the FG moiré and BG coincidence, but their intensity is distinctly different, the FG moiré being overwhelmed by the coincidence structure. Double scattering spots can be identified at high temperatures when the BG phase disappears (see Supporting Information). We note that graphene's diffraction beams display six-fold symmetry, which suggests that the film thickness is one layer.

Dark-field (DF) LEEM was used to correlate the LEED (low energy electron diffraction) pattern to the real-space surface structure. Representative images obtained using the first-order diffraction of graphene and the

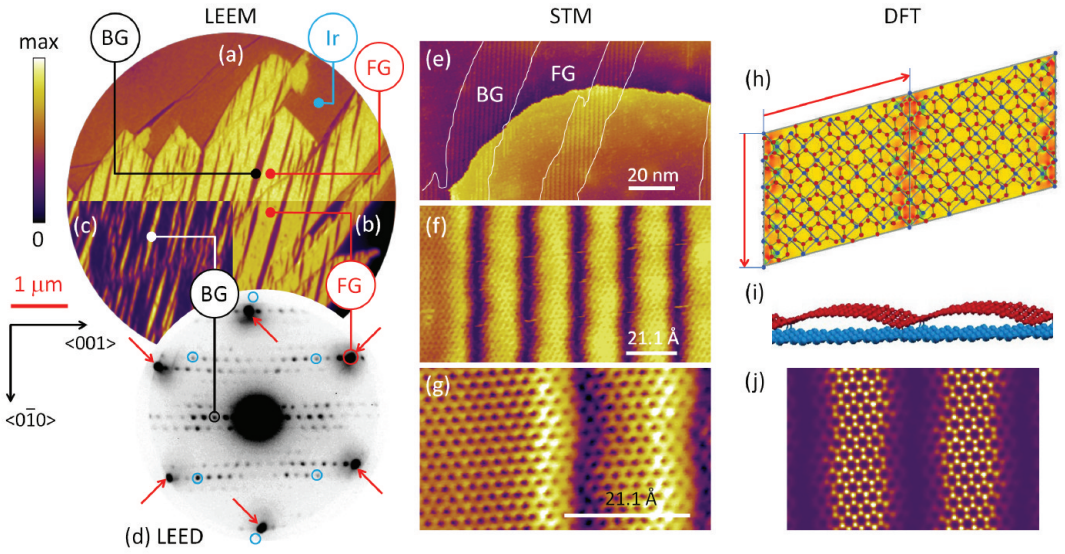

Figure 1. (Left panel) LEEM images of a graphene island at room temperature; principal crystallographic directions of Ir are indicated. (a) Bright-field LEEM at V_{start} = 12 eV; FG, BG, and Ir are identified by the corresponding labels. (b) Dark-field LEEM using FG first-order diffraction at V_{start} = 50 eV. (c) Dark-field LEEM using one of the superstructure beams, V_{start} = 12 eV. (d) Microprobe LEED on a similar island, V_{start} = 38 eV. The distortion is due to imperfect diffraction imaging conditions in our instrument. FG first-order spots are surrounded by the red arrows; for commodity, the blue circles mark the position of Ir first order spots on the unreconstructed (100) surface. (Middle panel) Large-area STM image of FG and BG domains (e), highlighted by the white contours (V_b = −300 mV, I_t = 1 nA). (f) STM image of the BG phase (V_b = 50 mV, I_t = 2 nA). (g) Atomic resolution image of BG, with FG on the left-hand side (V_b = −4 mV, I_t = 5 nA). (Right panel) Two contiguous BG unit cells (h), as determined by *ab initio* calculations. C atoms are indicated in red, Ir in blue; unit vectors (red) have been drawn sideways. The plot also shows the charge density difference between the BG phase and the noninteracting components (Ir slab + free graphene): green (orange) indicates positive (negative) charge differences, highlighting chemisorbed carbons (charge depletion). (i) Side view over BG, illustrating its large corrugation. For clarity, only the topmost Ir layer is shown. (j) Simulated STM image of BG at V_b = −4 mV.

coincidence structure beams are shown in Figure 1b,c, respectively. As can be seen, the dominant phase (FG) maps the extent of incommensurate graphene and the thin stripes (BG) that of the coincidence structure. The perfect complementarity between the two images, which can be appreciated by the evident inversion of contrast, further proves that the coincidence structure is not due to the moiré pattern accompanying the incommensurate graphene (FG), but rather to a different phase. The low energy electron reflectivity of the BG phase is lower than that of the FG phase, showing however almost identical dependence on the electron kinetic energy, which indicates a closely related crystal structure.

XPEEM (X-ray photoemission electron microscopy) measurements of the C 1s and Ir 4f core level emission (see the Supporting Information) allowed us to conclude that FG and BG have the same layer thickness and relatively similar atomic densities, BG surpassing FG by an estimated 2%. Both phases show a strong C 1s peak at 283.95 eV binding energy, a value that confirms their graphitic nature. The C 1s spectrum of BG shows a second smaller component, shifted at higher binding energy (284.7 eV) with respect to the main emission peak, suggesting the existence of a more strongly bound minority C species.

In order to characterize the atomic structure of the aforementioned graphene phases, we carried out STM measurements at high resolution. The wide-area image in Figure 1e illustrates the typical morphology of a single-layer graphene island at room temperature. As can be seen, few large domains showing flat morphology are separated by narrower regions resembling the stripe-shaped domains (BG) observed in LEEM. In STM at atomic resolution, both regions display the typical honeycomb hexagonal pattern of graphene, as can be seen in Figure 1g. Under appropriate conditions, a weak moiré pattern can be observed on the FG phase (see the Supporting Information), aligned parallel to the BG stripes, similar to the case of graphene on Cu(100).[28,29] The stripes observed in BG display, however, a much stronger contrast.

At closer inspection, the BG structure exhibits a perfectly regular texture consisting of nanometer-sized, one-dimensional nanostripes aligned to Ir⟨0$\bar{1}$0⟩, with a periodicity of 2.1 nm along Ir⟨001⟩ (Figure 1f,g). Note the intensity modulations also along the direction of the nanostripes, which create a sort of zigzag pattern with a period of 9 graphene rows. No appreciable variations in STM can be noticed when imaging empty or filled states, which suggests that these features are due to height variations (ripples) and not to electronic effects. The apparent distortion of the lattice observed close to the dark stripes indicates that these regions have the highest curvature. STM shows that the graphene lattice is continuous along Ir⟨001⟩, both across the stripes and across the transition from flat to

buckled regions; the lattice is evidently distorted at the end of the $\langle 0\bar{1}0\rangle$ termination of the dark stripes. Although no sharp boundaries are here observed, STM images cannot exclude the presence of isolated point defects or dislocations.

The above information, together with LEED, was used to determine the BG commensurate structure unit cell (see the Supporting Information), shown in Figure 1h. One of the unit vectors is aligned parallel to Ir$\langle 0\bar{1}0\rangle$, extending for 5 Ir lattice units (19.2 Å). The other forms an angle of about 15° with Ir$\langle 001\rangle$, with a length given by the sum of 5.5 $a^{Ir}_{\langle 001\rangle}$ (21.12 Å) and 1.5 $a^{Ir}_{\langle 0\bar{1}0\rangle}$ (5.76 Å). The simulation of the LEED pattern of the unit cell of BG matches the experimental data (see the Supporting Information). It is important to note that, due to the 3.5° rotation of the graphene unit vectors with respect to Ir$_{\langle 001\rangle}$, the diffraction spots of incommensurate graphene match closely those of the coincidence structure. The projected density of C atoms in the BG unit cell is 3.6% denser than that of FG, which corresponds reasonably well to the XPEEM estimate of 2%.

The equilibrium buckling and atomic positions within the unit cell of the new BG phase were determined theoretically. The side view of the cell in Figure 1i illustrates the exceptionally large buckling of the BG phase. Our GGA calculations show that the minimum and maximum separation between graphene and Ir are 1.9 and 4.0 Å, respectively, yielding a buckling of 2.1 Å. This buckling is significantly larger than any buckling previously found for chemisorbed graphene systems, including the largest GGA value calculated so far, that is, 1.5 Å for graphene/Ru(0001).[34] The experimental and simulated STM images in Figure 1g,j exhibit a striking similarity, corroborating the accuracy of the DFT results. The simulations confirm that the dark stripes observed in STM correspond to the part of the film which is closer to the surface. As the GGA calculations do not consider van der Waals interactions, we have also simulated the BG phase by applying the empirical dispersive corrections, within the DFT-D scheme.[35,36] As a result, the chemisorbed atoms closest to the surface are moved slightly further away from the surface to the distance of 2.1 Å, while the buckling is reduced to 1.7 Å.

The analysis of the calculated spatial distribution of the charge density, used to generate the color code in Figure 1h, indicates that only a small fraction of the C atoms, namely, 18 over 160 in the cell (*i.e.*, 11%), is actually chemisorbed to the Ir substrate, while the remaining part is physisorbed. On the experimental side, the high binding energy component in the C 1s spectrum of the BG phase can be ascribed to the chemisorbed atoms, based on an established interpretation of the photoemission spectrum of strongly and weakly bound C species.[10,12] The fit of the buckled phase C 1s spectrum, reported in the Supporting

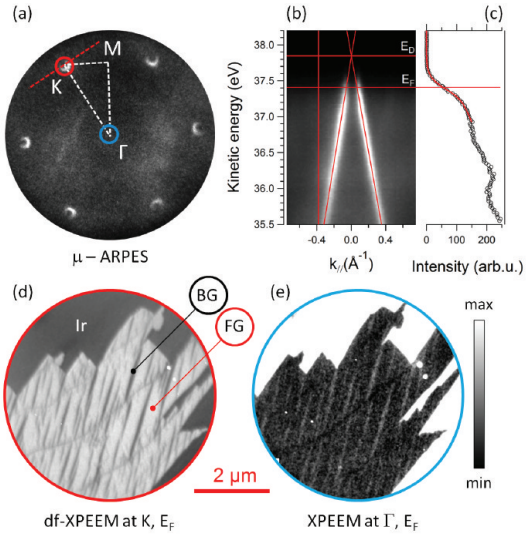

Figure 2. (a) μ-ARPES pattern of a graphene island on Ir(001) at room temperature; photon energy $h\nu$ = 40 eV; a start voltage of 36.4 eV was chosen in order to image E_F. Principal directions in the FBZ are indicated by the white dashed lines. (b) Cross section through one of the Dirac cones along a plane normal to $\Gamma-K$, as indicated by the red dashed line in (a). E_D was determined as the intersection point of the two red lines fitting the π band momentum distribution curves. (c) Intensity profile along the red vertical line in (b) and determination of E_F in a fit. (d) Dark-field XPEEM image of the same island shown in Figure 1. The image was obtained positioning an aperture at the *K* point in the diffraction plane, as indicated by the red circle in (a). The image intensity is proportional to the DOS close to K at E_F. (e) Normal emission XPEEM image at E_F. Image intensity is proportional to the DOS at Γ.

Information, shows that the chemisorbed atoms account for about 11 ± 4% (confidence interval of 68%) of the overall emission intensity, in very good agreement with theory. We conclude that the chemisorption of just a minor part of the C atoms dramatically alters the morphology of the film. As will be seen in the following, it also changes significantly the local electronic structure.

The electronic structure of flat and buckled graphene was characterized both experimentally and theoretically. Microprobe angle-resolved photoelectron spectroscopy (μ-ARPES) was employed to probe the dispersion of the π band at the Dirac cones within selected single-crystal graphene islands. A representative data set is shown in Figure 2a–c. The analysis of the momentum distribution curves confirmed linear dispersion close to the Fermi energy, E_F. Contrary to the case of Ir(111), where no significant doping is observed,[13] the Dirac point, E_D, is located at 0.42 ± 0.03 eV above E_F. The remarkable differences in the electronic properties of BG and FG phases were resolved due to a new experimental approach for angle-resolved photoemission electron microscopy, the dark-field (DF) method.[37] The DF-XPEEM micrograph in Figure 2d was obtained by imaging emission from graphene's π band at the reciprocal space *K* point, selected by positioning an aperture

in the diffraction plane. Since the ARPES intensity is proportional to the density of states (DOS), DF-PEEM enables a direct comparison of the local electronic structures. As can be seen in Figure 2d, only the FG shows up with high intensity. At the same time, the very low image intensity observed in the stripe-shaped areas suggests that the Dirac cones are disrupted in buckled graphene. We thus conclude that the μ-ARPES data in Figure 2a,b are only representative of the band structure of the FG phase. Notably, the BG phase exhibits slightly higher DOS at Γ, as demonstrated by the inversion of contrast in Figure 2e, pointing to a strong hybridization with the Ir states.

The above experimental observations are substantiated by DFT DOS calculations. In addition to the BG phase, we have also considered a physisorbed flat graphene film strained to the commensurate graphene/Ir unit cell of BG (a commensurate interface is a prerequisite for the atomistic simulations employing periodic boundary conditions). In our calculations for the physisorbed graphene film, the surface strain caused by the matching condition to the theoretical Ir lattice corresponds to a surface area contraction of 0.6% relative to the free-standing graphene monolayer. Theoretical results for different graphene structures, including BG, strained FG, free-standing graphene, free-standing BG, and strained free-standing FG, are shown in Figure 3. As can be seen, free-standing graphene and physisorbed strained FG have very similar characteristics (topmost two panels). For physisorbed FG, $E_D \approx 0.5$ eV, in good agreement with our experiments and consistent with previous calculations for other metals.[38] The calculated DOS of free-standing strained graphene (bottom panel) exhibits similar structures as the FG phase, but there is no shift of the Dirac point. This observation shows that the doping in the calculated FG DOS is not an artifact related to the strain used in our model unit cell, and thus confirms that it is due to the interaction with the Ir substrate. BG (middle panel) displays nonzero DOS at the Dirac point, indicating that the typical features of graphene's π band, with linear dispersion at the cones and zero DOS at E_D, are lost. This behavior is not observed for free-standing BG (second panel from bottom), that is, our buckled graphene without the Ir substrate. This is an important result, which confirms that the nonzero DOS of BG at the Dirac point does not originate from strain or rippling but from the chemisorption to the substrate. The disruption of Dirac cones due to strong substrate interaction is well-known for Ru;[14] on Ni, it is a debated subject,[22] with recent experiments indicating that E_D is shifted as much as 2.8 eV below the Fermi level.[21] The novel aspect highlighted in our study is that the change in the graphene DOS at the Dirac point, from semimetal to metallic-like, can be induced by the chemisorption of just a small fraction of the atoms in the unit cell (11%).

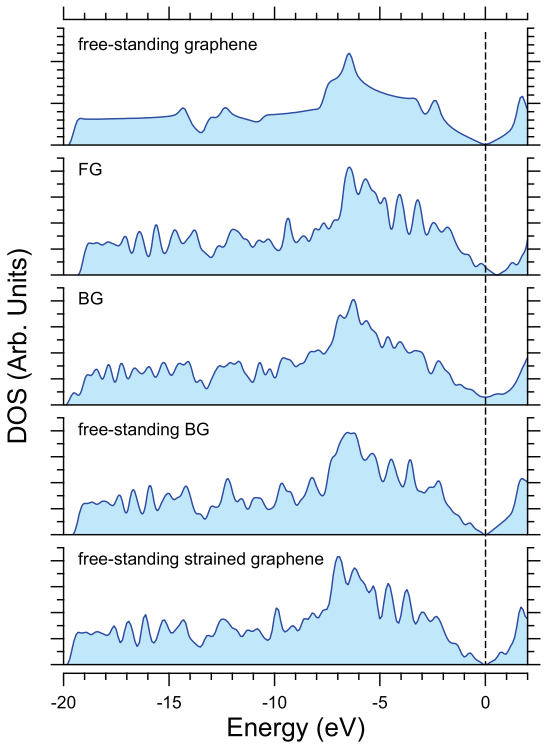

Figure 3. DFT calculations for the density of states (DOS) of different graphene structures. From top to bottom: free-standing graphene; physisorbed flat graphene (FG) strained to the BG unit cell; chemisorbed buckled graphene (BG); free-standing buckled graphene, *i.e.*, the BG structure without the Ir substrate; strained free-standing graphene, *i.e.*, a strained suspended graphene forced to fit to the unit cell of the BG phase. The topmost and two bottom panels describe, therefore, the DOS calculated for a single graphene layer without Ir substrate. The Fermi level is placed at 0 eV.

Another striking feature of the graphene/Ir(100) system is that the buckled structure can be *reversibly* transformed into flat graphene. The LEEM images in Figure 4a illustrate the phase transformation during annealing from room temperature to high temperatures and subsequent cooling. The dark stripes correspond to BG and the bright regions to FG. Comparison of the first and last image in the sequence shows that the restored BG stripes do not form at the initial locations but in different places. Further, the observation of stripes propagating across step bunches indicates that the development of the BG phase is not significantly influenced by the substrate morphology. Our LEEM data indicate that the phase transformation occurs in the temperature range from about 250 °C up to about 500 °C (see Figure 4c), following a linear trend. Upon cooling to ambient temperature, the coverage of BG phase in the LEEM images increases steadily, to saturate around a value of ~25% in Figure 4c. LEEM observations are in agreement with STM experiments at variable temperature, which did not show BG domains (identified by the characteristic nanostripes) above 500 °C (see Figure 4b), although few isolated rows of chemisorbed C adatoms were occasionally detected.

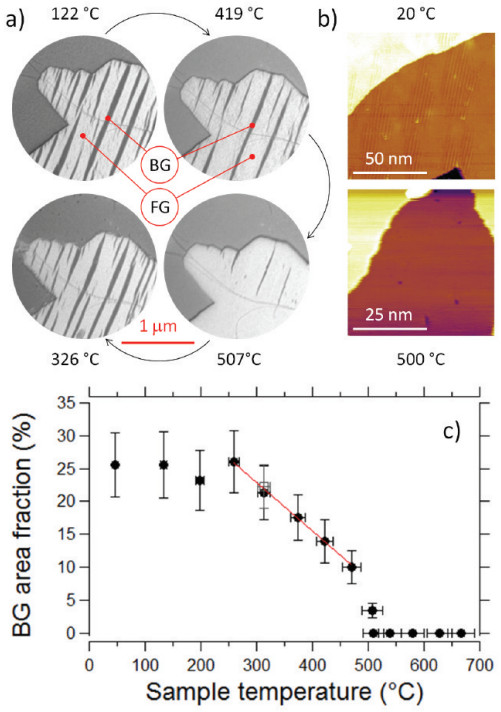

Figure 4. (a) Sequence of selected bright-field LEEM images (V_{start} = 16 eV) illustrating the phase BG−FG transformation during annealing and subsequent cooling. The dark stripes correspond to BG, the bright regions to FG. The arrows indicate the time direction. (b) STM images of graphene at room temperature and 500 °C. Image size: 100 nm × 100 nm and 50 nm × 50 nm, respectively; V_b = +50 mV, I_t = 1 nA, for both images. (c) Fractional coverage of the BG phase *versus* temperature from the analysis of LEEM data evaluating the area fraction of the dark stripes within a given graphene island. Filled circles represent annealing, empty squares a subsequent cooling. The fit (red line) serves as a guideline to identify the temperature range where the area fraction variation follows a linear trend. The error bars correspond to the area of blurred contour surrounding each BG domain, due to the lateral resolution of the microscope.

The reversibility of the BG−FG transition suggests that the film adapts its morphology to a changing external stimulus, which acts as a driving force for this process. We identify this driving mechanism as the elastic forces at the interface. It is well-known that creation of corrugations in graphene can relieve the strain resulting from the different expansion of substrate and film. A few notable examples have been reported in the literature: temperature-dependent ripple formations are observed in free-standing graphene membranes supported on SiO_2 trenches.[39] Branched wrinkles reversibly appear and disappear in cooling and annealing cycles in epitaxial graphene grown on Pt(111) and Ir(111).[40] A recent electron diffraction study on graphene/Ir(111) has elegantly demonstrated that wrinkle formation is closely correlated to hysteretic variations in the graphene lattice parameter. Further, it was found that this is an activated process, with a reported energy barrier as low as 1 eV/nm.[41] Besides the generality of the stress-releasing argument, rippling occurs in radically different manners on the (111) and (100) faces of Ir. On Ir(111), narrow and tall wrinkles form far from each other, organized into a network with random orientations.[40] Conversely, our observations on Ir(100) show that the ripples have regular nanometer spacing and fixed orientation, forming mesoscopic domains of a new denser chemisorbed phase that alternates with regions of perfectly flat physisorbed graphene.

The mechanistic process leading to the formation of ripples in graphene on Ir(100) deserves special attention and can be described as follows. At high temperatures, due to the high amplitude of lattice vibrations, graphene is mainly physisorbed to the substrate. However, the rolling carpet growth observed in LEEM experiments supports the picture that the film is already pinned at the substrate's step bunches. With decreasing temperature, further chemisorption to the substrate occurs initially at defects and film edges, due to their enhanced reactivity.[42,43] This is qualitatively confirmed by high-temperature STM measurements, which show a general tendency of the graphene edges to bend toward the substrate. Such bonds provide a stable anchorage for the film, inhibiting sliding. As a result, compressive strain arises in graphene, due to the mismatch in the thermal expansion coefficients of film and substrate. In fact, during cooling to ambient temperature, graphene slightly expands,[44] while Ir contracts markedly, with a lattice parameter (surface area) change of ~0.4% (0.8%) from 800 to 250 °C.[45] Thus, the graphene can become more corrugated, which, in turn, might favor chemisorption in the regions of increased curvature.[46,47] Interestingly, in order to release the strain induced by the substrate contraction, graphene organizes into alternating phases of different C surface densities that extend on mesoscopic lengths: one of them, the BG phase, is characterized by a C density increase of 3.6% relative to the unstrained graphene layer, a value that is notably larger than the 0.8% surface contraction imposed on the entire island by the mismatch accumulated during cooling. In this way, the other phase (FG) is left flat and mainly unstrained or only weakly strained. Thus, it can be deduced that the change of strain is mostly accommodated by varying the fractional coverage of the denser BG phase, rather than the ripple amplitude or period. In fact, conservation of mass allows us to roughly predict the proportion between the unstrained FG and the denser BG. By imposing an average density increase of 0.8% when cooling graphene from 800 to 250 °C and assuming FG is essentially unstrained, we obtain a rough estimate of the BG fractional area of 22% (see Supporting Information), in good agreement with the experimental results. Upon further cooling from 250 °C to room temperature, presumably for kinetic reasons, the system cannot change the proportion of the BG phase, despite the increase of strain. The additional strain at that point most likely compresses in equal

measure both the BG and FG parts of the graphene-covered surface.

The scenario of the strain release as driving force for the formation of the BG phase is supported by our *ab initio* calculations for FG and BG, which show that the strain of 0.8% imposed by the different thermal contraction/expansion will not be fully accommodated by FG. Indeed, both GGA and DFT-D calculations on the FG phase strained to the unit cell of BG (0.6% contraction strain) place it higher in energy than BG (in GGA by 0.05 eV per BG unit cell and in DFT-D by 1.68 eV per BG unit cell). This is in full agreement with the mechanism responsible for the creation of the BG phase, on the basis of which it can be expected that the energy of the thermally strained FG phase should be higher than the weighted average of the BG and equilibrium FG energies, as detailed in the Supporting Information.

We would like also to emphasize that the difference in density between FG and BG is anisotropic: we obtain values of approximatively 1.2% and 3.4% along $Ir_{\langle 0\bar{1}0\rangle}$ and $Ir_{\langle 001\rangle}$, respectively. Due to the isotropic contraction of the substrate, mass conservation determines the boundary orientation angle θ according to the ratio of the axial density change along the two main crystallographic directions: $\theta_{Ir\langle 001\rangle} = \tan^{-1}(\Delta n_i/\Delta n_j)$, where Δn_i and Δn_j are the density change along the $\langle 001\rangle$ and $\langle 0\bar{1}0\rangle$ directions, respectively. In our case, $\theta_{Ir\langle 001\rangle}$ corresponds to an angle of about 70° with respect to $Ir\langle 001\rangle$, in excellent agreement with experiment.

Coming eventually to discuss the periodicity of graphene ripples, the exact prediction of the wavelength is a very complex task requiring lengthy calculations, going beyond the scope of this work. In general, however, one may expect the strain to drive the formation of a rippled phase whose coincidence period is roughly determined by the energy balance between the ripple formation energy and the energy gained by the chemisorption to the substrate. The exact period, however, should warrant a convenient match between the film and the substrate lattices.

CONCLUSIONS

Our study demonstrates that the complex interfacial interactions arising between graphene and a support with non-three-fold symmetry have a crucial role in shaping the film morphology and its electronic properties. One of the novel and most striking aspects of our study on graphene/Ir(100) is that a reduced number of Ir−C chemisorption bonds can radically alter both the film morphology and its electronic structure, *via* a reversible temperature-controlled phase transformation. Thus, the temperature can be used as a switch to induce or remove rippling, achieving also very accurate control on the relative coverage of the flat and buckled graphene. Notably, our *ab initio* calculations have shown clearly that rippling or strain alone are not sufficient to significantly modify the quasi-particle dispersion. On the contrary, the onset of just a few interfacial chemisorption bonds is found to change the graphene DOS at the Dirac point from semimetal-like to metallic type. Such bonding mechanism provides the highest flexibility in controlling graphene electronic properties, allowing one to preserve or disrupt *ad libitum* the characteristics of the π band. Interface strain, originated by the different expansion coefficient of film and substrate, is the driving force inducing these changes, indeed a very general one. For this reason, we expect that one-dimensional ripples showing high degree of order might be observed in a multitude of sp^2-bonded layers supported on square or rectangular symmetry surfaces. In this regard, we highlight the potential of the buckled graphene phase as a model system. With exceptionally large one-dimensional ripples with a periodicity of 2.1 nm, it is indeed an ideal candidate substrate for synthesizing one-dimensional graphene-supported nanostructures exhibiting exotic physical and chemical properties.

METHODS

Sample Preparation. Bulk clean Ir(001) single crystals with miscut less than 0.1° (Surface Preparation Laboratory) were used in both LEEM and STM experiments. The Ir surface was prepared by repeated cycles of Ar sputtering (3×10^{-5} mbar, 1 kV) followed by annealing to 750 °C and treatment in 5×10^{-7} mbar O_2. In order to remove oxygen, the surface was flashed to 1200 °C before experiments. Upon cooling to room temperature, the surface developed a sharp (1×5) LEED pattern.

XPEEM and LEEM Measurements. The photoemission microscopy measurements were carried out using the spectroscopic photoemission and low energy electron microscope (SPELEEM) at the Elettra Synchrotron Light Laboratory.[48] This instrument combines low energy electron microscopy[31] with energy-filtered X-ray photoemission microscopy.[49] In the SPELEEM, the electron kinetic energy is controlled by biasing the sample with a negative potential. This bias is referred to as start voltage, V_{start}. The kinetic energy of the electrons scattered (or emitted) by the sample is equal to $E_{kin} = V_{start} - \delta W_{i-s}$, the latter being the difference in work function between the instrument and the specimen. In our measurements, LEEM was used in both bright- and dark-field modes, respectively, utilizing the first or secondary order diffraction beam for imaging. The microscope lateral resolution approaches a few tens of nanometers; energy resolution is better than 0.3 eV. Along with imaging, the SPELEEM allows diffraction operation mode. Depending whether the beamline photons or low energy electrons are used as probe, μ-ARPES or LEED measurements can be also carried out. The probed area, about 2 μm in diameter, is chosen by inserting a field limiting or illumination aperture in the optical path of the instrument. Part of the ARPES measurements was made utilizing the dark-field PEEM method.[37] In the LEEM experiments, the sample temperature was measured with an S-type thermocouple and checked with an optical pyrometer.

Scanning Tunneling Microscopy Measurements. STM images were acquired with a modified Omicron variable-temperature STM (VT-STM) in the 300−780 K temperature (T) range. Imaging was performed in constant-current mode with tunneling current (I_t)

ranging from 1 to 5 nA and bias voltage (V_b) ranging from 2 to 800 mV for both empty ($V_b > 0$) and filled ($V_b < 0$) states. Specific T, I_t, and V_b values are reported for each image in the figure captions.

DFT Calculations. The DFT calculations were performed using the pseudopotential plane-wave method, as implemented in the PWSCF code, a part of the Quantum ESPRESSO distribution.[50] The generalized-gradient approximation (GGA) in the Perdew–Burke–Ernzerhof parametrization[51] was adopted for the exchange and correlation functional. Surfaces were modeled using slab geometry in a periodically repeated supercell. The slab consists of three atomic layers of Ir, terminated on one side with a graphene layer. A vacuum layer separates the two periodic images of the slab, with a spacing of 14 Å between the two Ir slab replicas. Our supercell contains 165 Ir and 160 C atoms. The atomic positions of the atoms in the graphene layer and in the adjacent Ir surface monolayer were allowed to relax. We used Vanderbilt ultrasoft pseudopotentials.[52] Our kinetic energy cutoff was 28 Ry for the wave functions and 320 Ry for the charge density. A $1 \times 1 \times 1$ k-point Monkhorst–Pack mesh was used for the total-energy calculations and a grid $2 \times 2 \times 1$ for the density of states, STM, and the charge density calculations. For the calculation of DOS for the free graphene, we constructed a two-atom unit cell with a $24 \times 24 \times 1$ k-point grid, resulting in different smoothness of the DOS curve with respect to the calculations performed in the BG unit cell. We employed a Gaussian level smearing of 0.02 Ry. The calculations were performed with the theoretical Ir lattice constant of 3.90 Å, which is 1.5% different from the experimental lattice constant of 3.84 Å. We note that our graphene lattice parameter is virtually identical to the experimental one. For comparison, in some cases, we also performed DFT-D calculations to empirically take into account van der Waals interactions.[35] The carbon C_6 parameter used for the calculations was taken from ref 36; for Ir, the C_6 coefficient was determined by comparing DFT-D and nonlocal vdW-DF calculations on the adsorption of graphene on Ir(100). The same k-point grids and cutoffs as for the GGA calculations were used.

Conflict of Interest: The authors declare no competing financial interest.

Acknowledgment. C.A. acknowledges financial support from CNR, through the ESF FANAS project NOMCIS, and from MIUR (PRIN 2010-2011 No. 2010N3T9M4). The help of Carlo Dri and Friedrich Esch (design) and Paolo Bertoch and Federico Salvador (manufacturing) in the realization of the high-temperature STM sample holder is gratefully acknowledged. A.L. thanks Federico Morelli for help in the analysis of the BG area fraction.

Supporting Information Available: Laterally resolved XPEEM measurements on the flat and buckled graphene phases on Ir(100), the STM and LEED determination of the unit cell of buckled graphene, some aspects of the *ab initio* calculations for this system, and also a criterion for the prediction of the buckled graphene area fraction. This material is available free of charge *via* the Internet at http://pubs.acs.org.

REFERENCES AND NOTES

1. Geim, A. K.; Novoselov, K. S. The Rise of Graphene. *Nat. Mater.* **2007**, *6*, 183–191.
2. Castro Neto, A. H.; Guinea, F.; Peres, N. M. R.; Novoselov, K. S.; Geim, A. K. The Electronic Properties of Graphene. *Rev. Mod. Phys.* **2009**, *81*, 109–162.
3. Hupalo, M.; Liu, X.; Wang, C.-Z.; Lu, W.-C.; Yao, Y.-X.; Ho, K.-M.; Tringides, M. C. Metal Nanostructure Formation on Graphene: Weak *versus* Strong Bonding. *Adv. Mater.* **2011**, *23*, 2082–2087.
4. N'Diaye, A. T.; Bleikamp, S.; Feibelman, P. J.; Michely, T. Two-Dimensional Ir Cluster Lattice on a Graphene Moiré on Ir(111). *Phys. Rev. Lett.* **2006**, *97*, 215501.
5. Lee, E. J. H.; Balasubramanian, K.; Weitz, R. T.; Burghard, M.; Kern, K. Contact and Edge Effects in Graphene Devices. *Nat. Nanotechol.* **2008**, *3*, 486–490.
6. Schwierz, F. Graphene Transistors. *Nat. Nanotechol.* **2010**, *5*, 487–496.
7. Böhm, H. P.; Clauss, A.; Hofmann, U.; Fischer, G. O. Dunnste Kohlenstof-Folien. *Z. Naturforsch. B* **1962**, *17*, 150–153.
8. Rut'kov, E. V.; Gall, N. R. Equilibrium Nucleation, Growth, and Thermal Stability of Graphene on Solids. In *Physics and Applications of Graphene-Experiments*; Mikhailov, S., Ed.; InTech, 2011.
9. Batzill, M. The Surface Science of Graphene: Metal Interfaces, CVD Synthesis, Nanoribbons, Chemical Modifications, and Defects. *Surf. Sci. Rep.* **2012**, *67*, 83–115.
10. Preobrajenski, A. B.; Ng, M. L.; Vinogradov, A. S.; Mårtensson, N. Controlling Graphene Corrugation on Lattice-Mismatched Substrates. *Phys. Rev. B* **2008**, *78*, 073401.
11. Moritz, W.; Wang, B.; Bocquet, M.-L.; Brugger, T.; Greber, T.; Wintterlin, J.; Günther, S. Structure Determination of the Coincidence Phase of Graphene on Ru(0001). *Phys. Rev. Lett.* **2010**, *104*, 136102.
12. Miniussi, E.; Pozzo, M.; Baraldi, A.; Vesselli, E.; Zhan, R. R.; Comelli, G.; Menteş, T. O.; Niño, M. A.; Locatelli, A.; Lizzit, S.; *et al.* Thermal Stability of Corrugated Epitaxial Graphene Grown on Re(0001). *Phys. Rev. Lett.* **2011**, *106*, 216101.
13. Pletikosić, I.; Kralj, M.; Pervan, P.; Brako, R.; Coraux, J.; N'Diaye, A. T.; Busse, C.; Michely, T. Dirac Cones and Minigaps for Graphene on Ir(111). *Phys. Rev. Lett.* **2009**, *102*, 056808.
14. Sutter, P.; Hybertsen, M. S.; Sadowski, J. T.; Sutter, E. Electronic Structure of Few-Layer Epitaxial Graphene on Ru(0001). *Nano Lett.* **2009**, *9*, 2654–2660.
15. Busse, C.; Lazić, P.; Djemour, R.; Coraux, J.; Gerber, T.; Atodiresei, N.; Caciuc, V.; Brako, R.; N'Diaye, A. T.; Blügel, S.; *et al.* Graphene on Ir(111): Physisorption with Chemical Modulation. *Phys. Rev. Lett.* **2011**, *107*, 036101.
16. Man, K. L.; Altman, M. S. Low Energy Electron Microscopy and Photoemission Electron Microscopy Investigation of Graphene. *J. Phys.: Condens. Matter* **2012**, *24*, 314209.
17. Giovannetti, G.; Khomyakov, P. A.; Brocks, G.; Karpan, V. M.; van den Brink, J.; Kelly, P. J. Doping Graphene with Metal Contacts. *Phys. Rev. Lett.* **2008**, *101*, 026803.
18. Varykhalov, A.; Scholz, M. R.; Kim, T. K.; Rader, O. Effect of Noble-Metal Contacts on Doping and Band Gap of Graphene. *Phys. Rev. B* **2010**, *82*, 121101.
19. Gao, M.; Pan, Y.; Zhang, C.; Hu, H.; Yang, R.; Lu, H.; Cai, J.; Du, S.; Liu, F.; Gao, H.-J. Tunable Interfacial Properties of Epitaxial Graphene on Metal Substrates. *Appl. Phys. Lett.* **2010**, *96*, 053109.
20. Sutter, P.; Sadowski, J. T.; Sutter, E. A. Chemistry under Cover: Tuning Metal-Graphene Interaction by Reactive Intercalation. *J. Am. Chem. Soc.* **2010**, *132*, 8175–8179.
21. Varykhalov, A.; Marchenko, D.; Sánchez-Barriga, J.; Scholz, M. R.; Verberck, B.; Trauzettel, B.; Wehling, T. O.; Carbone, C.; Rader, O. Intact Dirac Cones at Broken Sublattice Symmetry: Photoemission Study of Graphene on Ni and Co. *Phys. Rev. X* **2012**, *2*, 041017.
22. Sun, J.; Hannon, J. B.; Tromp, R. M.; Johari, P.; Bol, A. A.; Shenoy, V. B.; Pohl, K. Spatially-Resolved Structure and Electronic Properties of Graphene on Polycrystalline Ni. *ACS Nano* **2010**, *4*, 7073–7077.
23. Kozlov, S. M.; Viñes, F.; Görling, A. Bonding Mechanisms of Graphene on Metal Surfaces. *J. Phys. Chem. C* **2012**, *116*, 7360–7366.
24. Wofford, J. M.; Nie, S.; McCarty, K. F.; Bartelt, N. C.; Dubon, O. D. Graphene Islands on Cu Foils: the Interplay between Shape, Orientation, and Defects. *Nano Lett.* **2010**, *10*, 4890–4896.
25. Walter, A. L.; Nie, S.; Bostwick, A.; Kim, K. S.; Moreschini, L.; Chang, Y. J.; Innocenti, D.; Horn, K.; McCarty, K. F.; Rotenberg, E. Electronic Structure of Graphene on Single-Crystal Copper Substrates. *Phys. Rev. B* **2011**, *84*, 195443.
26. Vinogradov, N. A.; Zakharov, A. A.; Kocevski, V.; Rusz, J.; Simonov, K. A.; Eriksson, O.; Mikkelsen, A.; Lundgren, E.; Vinogradov, A. S.; Mårtensson, N.; *et al.* Formation and Structure of Graphene Waves on Fe(110). *Phys. Rev. Lett.* **2012**, *109*, 026101.
27. Cho, J.; Gao, L.; Tian, J.; Cao, H.; Wu, W.; Yu, Q.; Yitamben, E. N.; Fisher, B.; Guest, J. R.; Chen, Y. P.; *et al.* Atomic-Scale Investigation of Graphene Grown on Cu Foil and the

Effects of Thermal Annealing. *ACS Nano* **2011**, *5*, 3607–3613.
28. Rasool, H. I.; Song, E. B.; Mecklenburg, M.; Regan, B. C.; Wang, K. L.; Weiller, B. H.; Gimzewski, J. K. Atomic-Scale Characterization of Graphene Grown on Copper (100) Single Crystals. *J. Am. Chem. Soc.* **2011**, *133*, 12536–12543.
29. Zhao, L.; Rim, K.; Zhou, H.; He, R.; Heinz, T.; Pinczuk, A.; Flynn, G.; Pasupathy, A. Influence of Copper Crystal Surface on the CVD Growth of Large Area Monolayer Graphene. *Solid State Commun.* **2011**, *151*, 509–513.
30. Vinogradov, N. A.; Zakharov, A. A.; Ng, M. L.; Mikkelsen, A.; Lundgren, E.; Mårtensson, N.; Preobrajenski, A. B. One-Dimensional Corrugation of the h-BN Monolayer on Fe(110). *Langmuir* **2012**, *28*, 1775–1781.
31. Bauer, E. Low Energy Electron Microscopy. *Rep. Prog. Phys.* **1994**, *57*, 895.
32. Altman, M. S. Trends in Low Energy Electron Microscopy. *J. Phys.: Condens. Matter* **2010**, *22*, 084017.
33. Loginova, E.; Bartelt, N. C.; Feibelman, P. J.; McCarty, K. F. Factors Influencing Graphene Growth on Metal Surfaces. *New J. Phys.* **2009**, *11*, 063046.
34. Martoccia, D.; Willmott, P. R.; Brugger, T.; Björck, M.; Günther, S.; Schlepütz, C. M.; Cervellino, A.; Pauli, S. A.; Patterson, B. D.; Marchini, S.; *et al.* Graphene on Ru(0001): A 25 × 25 Supercell. *Phys. Rev. Lett.* **2008**, *101*, 126102.
35. Barone, V.; Casarin, M.; Forrer, D.; Pavone, M.; Sambi, M.; Vittadini, A. Role and Effective Treatment of Dispersive Forces in Materials: Polyethylene and Graphite Crystals as Test Cases. *J. Comput. Chem.* **2009**, *30*, 934–939.
36. Grimme, S. Semiempirical GGA-Type Density Functional Constructed with a Long-Range Dispersion Correction. *J. Comput. Chem.* **2006**, *27*, 1787–1799.
37. Mentes, T. O.; Locatelli, A. Angle-Resolved X-ray Photoemission Electron Microscopy. *J. Electron Spectrosc. Relat. Phenom.* **2012**, *185*, 323–329.
38. Khomyakov, P. A.; Giovannetti, G.; Rusu, P. C.; Brocks, G.; van den Brink, J.; Kelly, P. J. First-Principles Study of the Interaction and Charge Transfer between Graphene and Metals. *Phys. Rev. B* **2009**, *79*, 195425.
39. Bao, W.; Miao, F.; Chen, Z.; Zhang, H.; Jang, W.; Dames, C.; Lau, C. N. Controlled Ripple Texturing of Suspended Graphene and Ultrathin Graphite Membranes. *Nat. Nanotechol.* **2009**, *4*, 562–566.
40. N'Diaye, A. T.; van Gastel, R.; Martínez-Galera, A. J.; Coraux, J.; Hattab, H.; Wall, D.; Meyer zu Heringdorf, F.-J.; Horn-von Hoegen, M.; Gómez-Rodríguez, J.; Poelsema, B.; *et al. In Situ* Observation of Stress Relaxation in Epitaxial Graphene. *New J. Phys.* **2009**, *11*, 113056.
41. Hattab, H.; N'Diaye, A. T.; Wall, D.; Klein, C.; Jnawali, G.; Coraux, J.; Busse, C.; van Gastel, R.; Poelsema, B.; Michely, T.; *et al.* Interplay of Wrinkles, Strain, and Lattice Parameter in Graphene on Iridium. *Nano Lett.* **2012**, *12*, 678–682.
42. Banhart, F.; Kotakoski, J.; Krasheninnikov, A. V. Structural Defects in Graphene. *ACS Nano* **2011**, *5*, 26–41.
43. Malola, S.; Häkkinen, H.; Koskinen, P. Structural, Chemical, and Dynamical Trends in Graphene Grain Boundaries. *Phys. Rev. B* **2010**, *81*, 165447.
44. Mounet, N.; Marzari, N. First-Principles Determination of the Structural, Vibrational and Thermodynamic Properties of Diamond, Graphite, and Derivatives. *Phys. Rev. B* **2005**, *71*, 205214.
45. Halvorson, J. J.; Wimber, R. T. Thermal Expansion of Iridium at High Temperatures. *J. Appl. Phys.* **1972**, *43*, 2519–2522.
46. Fan, X.; Nouchi, R.; Tanigaki, K. Effect of Charge Puddles and Ripples on the Chemical Reactivity of Single Layer Graphene Supported by SiO_2/Si Substrate. *J. Phys. Chem. C* **2011**, *115*, 12960–12964.
47. Boukhvalov, D. W.; Katsnelson, M. I. Enhancement of Chemical Activity in Corrugated Graphene. *J. Phys. Chem. C* **2009**, *113*, 14176–14178.
48. Locatelli, A.; Aballe, L.; Mentes, T. O.; Kiskinova, M.; Bauer, E. Photoemission Electron Microscopy with Chemical Sensitivity: SPELEEM Methods and Applications. *Surf. Interface Anal.* **2006**, *38*, 1554–1557.
49. Schmidt, T.; Heun, S.; Slezak, J.; Diaz, J.; Prince, K. C.; Lilienkamp, G.; Bauer, E. SPELEEM: Combining LEEM and Spectroscopic Imaging. *Surf. Rev. Lett.* **1998**, *5*, 1287–1296.
50. Giannozzi, P.; Baroni, S.; Bonini, N.; Calandra, M.; Car, R.; Cavazzoni, C.; Ceresoli, D.; Chiarotti, G. L.; Cococcioni, M.; Dabo, I.; *et al.* QUANTUM ESPRESSO: A Modular and Open-Source Software Project for Quantum Simulations of Materials. *J. Phys.: Condens. Matter* **2009**, *21*, 395502.
51. Perdew, J. P.; Burke, K.; Ernzerhof, M. Generalized Gradient Approximation Made Simple. *Phys. Rev. Lett.* **1996**, *77*, 3865–3868.
52. Vanderbilt, D. Soft Self-Consistent Pseudopotentials in a Generalized Eigenvalue Formalism. *Phys. Rev. B* **1990**, *41*, 7892–7895.